Acta Materialia 220 (2021) 117336

Contents lists available at ScienceDirect

Acta Materialia

journal homepage: www.elsevier.com/locate/actamat

Strong strain gradients and phase coexistence at the metal-insulator transition in VO_2 epitaxial films

Laura Rodríguez[a], Felip Sandiumenge[b], Carles Frontera[b], José Manuel Caicedo[a], Jessica Padilla[a], Gustau Catalán[a,c], José Santiso[a,*]

[a] Catalan Institute of Nanoscience and Nanotechnology, ICN2, CSIC and The Barcelona Institute of Science and Technology (BIST), Campus UAB, 08193 Bellaterra, Barcelona. Spain
[b] Institut de Ciència de Materials de Barcelona (ICMAB-CSIC). Campus UAB, 08193 Bellaterra, Catalonia. Spain
[c] ICREA - Institució Catalana de Recerca i Estudis Avançats, 08010 Barcelona, Catalonia. Spain

ARTICLE INFO

Article history:
Received 25 June 2021
Revised 8 September 2021
Accepted 15 September 2021
Available online 26 September 2021

Keywords:
Metal-insulator transitions
Phase coexistence
Martensitic transitions
Local strain fields

ABSTRACT

The proximity of a thermodynamic triple point and the formation of transient metastable phases may result in complex phase and microstructural trajectories across the metal-insulator transition in strained VO_2 films. A detailed analysis using in-situ synchrotron X-ray diffraction unveils subtle fingerprints of this complexity in the structure of epitaxial films. During phase transition the low-temperature monoclinic M1 phase is constrained along the $\{111\}_R$ planes by the coexisting high-temperature R phase domains, which remain epitaxially clamped to the substrate. This geometrical constraint induces counteracting local stresses that result in a combined tilt and uniaxial in-plane compression of M1 domains, and a concomitant anomalous c_R-axis elongation. This mechanism progressively transforms the M1 phase into the transitional triclinic phase (T), and ultimately into the monoclinic M2 phase, generating strong strain and tilt gradients that remain frozen after the complete transformation of the R phase upon cooling to RT. The transformation path of VO_2 films, the complex competition between stable and metastable VO_2 polymorphs and its impact on the structure of the low temperature monoclinic state, provide essential insights for understanding the electronic and mechanical properties of the films at the nanoscale, as well as to control their use in functional devices.

1. Introduction

VO_2 is a strongly correlated electron material that in bulk form presents a first-order metal-insulator transition (MIT) at about 68 °C, with several orders of magnitude change in electrical conductivity as well as in infrared optical transmittance [1–4]. These properties make VO_2 attractive in applications like thermochromic smart windows [5] and in field-effect transistors [6–8]. The MIT is accompanied by a displacive structural transition from a low-temperature monoclinic phase (M1, with space group $P2_1/c$) to a high-temperature tetragonal conducting phase (isostructural to rutile R phase, space group $P4_2/mnm$). The most important structural feature of this transition, which relates to the electronic localization and the opening of a 0.6 eV gap, is the formation of two characteristic V-V distances along the c_R direction in the low-temperature M1 phase resulting from the alternate displacement of V ions from the central position of the VO_6 octahedra columns, forming zig-zag chains of dimers, while the high-temperature R phase consists of straight chains with equal V-V distances. However, it is well established that under uniaxial tensile strain along c_R-axis [9], or compressive uniaxial strain along the $[110]_R$ direction [10], there appears a monoclinic insulating phase, M2, consisting of two types of V chains parallel to the c_R direction alternating straight V-V dimers or zig-zag non-dimerized V chains. This separation into two different V-V chains results from the compression of one column set of VO_6 octahedra oriented with their axis connecting apical O atoms along the $[110]_R$ direction, while the other column set of VO_6 octahedra are longitudinally stretched along the $[1\text{-}10]_R$ direction. In equilibrium conditions, these three phases, M1, M2 and R, may coexist at the transition temperature in a solid-state triple point of the phase diagram [11,12]. Besides these polymorphs, there exist transient, metastable phases playing bridging roles between them, namely, 1) a triclinic (T) (also referred to as M3) phase forming at the transition between

* Corresponding author.
E-mail address: jose.santiso@icn2.cat (J. Santiso).

https://doi.org/10.1016/j.actamat.2021.117336

the M1 and M2 structures, [12–14], and 2) metallic monoclinic phases bridging the R and M1 structures [15–17], which, altogether, illustrate the complexity and adaptive nature of the VO_2 system.

The richness of the phase diagram, combined with the ferroelastic-martensitic character of VO_2, makes the pathway of the transformation from the low-temperature (M1) to the high-temperature (R) ground states strongly dependent on geometrical constraints and strain fields, which may induce different forms of phase coexistence and multiscale microstructures below and across the transition. There are multiple examples in the literature concerning the observation of mesoscale domains in VO_2 single crystals and epitaxial films consisting of various phases and different domain arrangements. For instance, in 2D nanoplatelets [18,19] and 1D nanobeams [20], different ferroelastic domain configurations have been reported which depend on the size and orientation of the crystals, as well as M1/R phase coexistence during the transition [21]. Even more complex scenarios are observed in nanobeams under stress, with the formation of the M2 polymorph at the interface between M1 and R domains during the transition [22–24]. Similar T and M2 domains were also observed in interfacial regions between M1 and R in polycrystalline films on Si_3N_4 membranes [25] or epitaxial films on $Al_2O_3(0001)$ substrates [26]. In epitaxial VO_2 films grown on $TiO_2(001)$ substrates experimental evidences reported so far, indicate that, due to the large cell parameter change during phase transition, films tend to generate microcracks as a strain relaxation mechanism [27–29]. As a consequence, it is observed that the phase and microstructural trajectories during the transition of $VO_2/TiO_2(100)$ films become spatially heterogeneous. In the proximity of the cracks, the film is relaxed, thus evolving from M1 ground state to R upon transition without intermediate phases [11,12,30]. On the other hand, the regions between cracks have been observed to retain an in-plane biaxial compressive strain up to thicknesses above 80nm [27,30]. Under such strain conditions the strain-Temperature phase diagram predicts the absence of intermediate phases between M1 and R phases during transition [11,12]. However, recent investigations by this group have shown that strained VO_2 films may develop very fine pre-transitional tweed textures prior to relaxation and condensation of the low temperature M1 ground state [17]. Such textures look tetragonal on average, and are promoted by the nucleation of a transient metallic monoclinic phase (x3M), and evolve with film thickness towards multicomponent tweeds incorporating the x3M, M1 and M2 structures on a rutile-like scaffold [17]. At that stage, the nanoscale phase intermixing of those domains precludes any differentiation of existing phases from X-ray diffraction experiments, since the peak commonly assigned to the rutile phase in fact encompasses variable levels of those polymorphs, macroscopically keeping an average tetragonal symmetry. During the transition, however, those bridging phases are expected to evolve, eventually growing in size, within measurable levels. Similarly, a recent review on VO_2 claim that local perturbations of the strain state induced by the presence of defects or ferroelastic domains may produce deviations from the expected equilibrium phases landscape [31]. The present study focusses on the temperature evolution of VO_2 film phase coexistence and microstructure by synchrotron X-ray diffraction in-situ analysis. Despite the inherent presence of microcracks in the films, the accurate study of the intensity distribution around the corresponding main Bragg positions allows to unravel a transformation path through adaptive distortions of the monoclinic phase upon the transition from the high-temperature rutile phase, involving the formation of T and M2 phase tilted domains. These distortions, which in fact result from varying degrees of V-V dimerization, remain frozen at room temperature in virtually perfect films of the low-temperature insulating M1 phase.

2. Experimental methods

VO_2 films were grown on $TiO_2(001)$ single crystal substrates by pulsed laser deposition from a V_2O_5 ceramic target. The ablation was performed by using a KrF excimer laser (Lambda Physik COMPex 201, λ= 248 nm wavelength). Film growth conditions were 400 °C deposition temperature, 10 mTorr gas pressure of pure O_2, laser fluence of 0.8 J•cm^{-2} and target-to-substrate distance of 55 mm. The cooling down step was at 15 °C•min^{-1} keeping the same gas pressure. All the samples shown in this work were grown under the same PLD growth conditions, with thicknesses between 40 nm up to 120 nm by varying the number of pulses (growth rate ~ 0.03 nm•pulse^{-1}). Films were analysed by XRD by using a 6-angle goniometer diffractometer at the KMC2 line at Helmholtz-Zentrum Berlin synchrotron radiation with a Vantec 2000 2D GADDS detector (with 2048 × 2048 pixels) at energy selected to λ=1.54 Å, as well as in a lab diffractometer with 4-angle goniometer (MRD X'Pert Pro from Malvern-Panalytical) and Cu Kα tube and 2 x Ge(110) monochromator. In both XRD setups the sample temperature was controlled by using a sample stage for non-ambient analysis (DHS1100C from Anton Paar). Slight temperature differences (± 5°C) could result from the different sample holder setup of both experiments.

We analysed a collection of VO_2 and TiO_2 HKL reflections by measuring conventional $2\theta/\omega$ scans and reciprocal 2D maps in the lab diffractometer. More detailed analysis of the reciprocal space reflections was performed by measuring 3D reciprocal space maps in the synchrotron source. The 3D maps were constructed by making use of the 2D information in each frame (2D detector) measured by scanning either different ϕ angles (azimuthal angle), or η angles (incidence angle). We chose reflections which contained information about out-of-plane cell parameters (such as 002_R), as well as in-plane components (112_R, 101_R, and $1/2\ 0\ 3/2_R$).

The evolution of the reflections with temperature was followed by heating at small steps starting from room temperature up to the completion of the phase transition (about 70 °C depending on the sample thickness). Measurements on synchrotron source with 2D detector provide a fast overview of the 3D reciprocal space even for weak reflections. However, peak positions depend on a careful sample alignment and detector calibration. For accurate lattice parameter determination, the 2D maps measured at diffractometer lab were used (Figure S6 and S7).

3. Results and discussion

All deposited films consist of pure VO_2 epitaxially oriented on $TiO_2(001)$ substrates, with the $[001]_R$ -axis perpendicular to the substrate plane, and $[100]/[010]_R$ directions parallel to the equivalent in-plane axes of the TiO_2 substrate. X-ray diffraction $2\theta/\omega$ scans at different temperatures, from 25 °C to 70 °C, are depicted in Fig. 1 a. They show the evolution of the 002 VO_2 film and TiO_2 substrate peaks during the phase transition for a 80 nm thick sample. Fig. 1b shows a characteristic electrical transport measurement of a similar film with a clear insulating to metal transition at about 50 °C, with a change of resistivity of more than two orders of magnitude. The transport curve presents some hysteretic behavior in the heating and cooling cycles as typically shown in MIT transitions.

The XRD scan obtained at 25 °C, below the transition, shows a broad peak with maximum at 2θ= 65.2°, and a shoulder on the left side of the peak. When heating up, at 35-40 °C a second maximum appears at 2θ= 65.7°. These two peaks correspond to the $40\bar{2}_{M1}$ and 002_R reflections of the monoclinic (M1) and rutile (R) VO_2 phases, respectively. Note that the monoclinic $40\bar{2}_{M1}$ reflection corresponds to the same 002_R orientation when expressed in the tetragonal setting of the parent rutile structure. At higher tem-

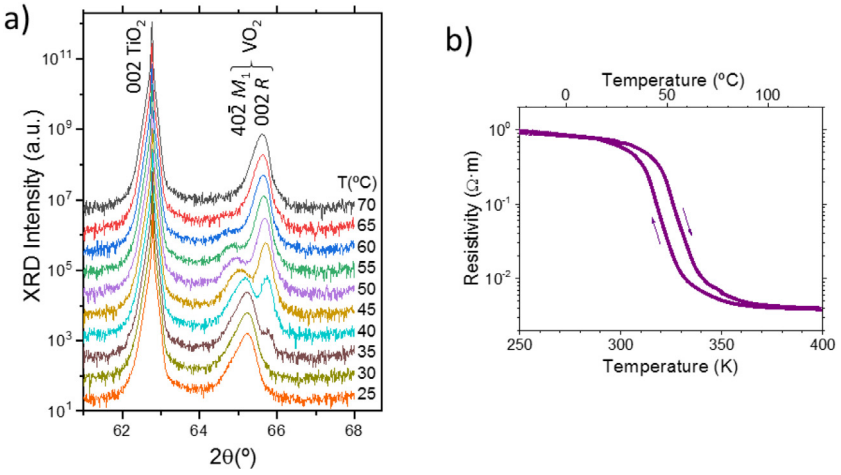

Fig. 1. (a) High resolution XRD $2\theta/\omega$ scans in the region of 002 TiO_2, $40\bar{2}_{M1}$ and 002_R VO_2 reflections for an 80 nm thick sample. (b) Resistivity versus temperature for a similar sample (60nm thick) showing the transition from the insulating to the metallic phase for heating and cooling cycles (indicated by arrows).

Table 1
Measured and reported pseudo-tetragonal lattice parameters for M1 and R phases

Phase	Lattice constants [Å]		Strain [%]	
	bulk	film	$\varepsilon_\perp$	$\varepsilon_{//}$
M1	c_R= 2.872 a_R= 4.516 // $[100]_R$ = 4.528 // $[010]_R$ [a)]	c_R= 2.858 a_R= 4.592 [c)]	- 0.5	+ 1.5
R	c_R= 2.860 a_R= 4.556 [b)]	c_R= 2.839 a_R= 4.592 [c)]	- 0.7	+ 0.78

a) from ref [37]; b) ref [14]; c) at this stage (40 °C) both phases are assumed to be fully strained to the substrate, so this value is taken from in-plane TiO_2(001) crystal

peratures, the monoclinic peak intensity decreases while the rutile intensity increases, and this progressive unbalance extends over a wide range of temperatures, from 35 to 55 °C, which approximately coincides with the transition range observed in the transport measurement.

At 40 °C, when the two coexisting phases yield about the same maximum intensity, the measured d_{002} interplanar distances correspond to the pseudo-rutile out-of-plane unit cell parameters 2.858 Å and 2.839 Å, for M1 and R phases, respectively, as shown in Table 1. These unit cell parameters are -0.5 % and -0.7 % shorter than reported bulk parameters, 2.872 Å for $(40\bar{2})$-oriented M1, and 2.860 Å for (001)-oriented R phases, respectively. This contraction results from the elastic response to the tensile in-plane biaxial stress of the VO_2 layer on the (001)TiO_2 single crystal substrate. Looking at the bulk in-plane unit cell parameters of the reported M1 phase, 4.516 Å and 4.528 Å, along the $[100]_R$ and $[010]_R$ pseudo-tetragonal rutile directions (average in-plane value is 4.522 Å), the average mismatch is about +1.5 %, while for rutile VO_2, it is about +0.78 %. The large difference between the mismatch of the M1 and R phases induces the formation of microcracks above a critical thickness of about 15 nm, as previously reported. [27–29] and also discussed in the supplementary information (Fig. S9).

3.1. Evolution of lattice distortions during the phase transition

A deeper insight into the evolving VO_2 microstructure was obtained by performing XRD 3D reciprocal space maps during heating from room temperature up to 50 °C across the phase transition on a 120 nm thick film. Since the distortions analyzed in this work produce only weak diffuse signatures around main reflections, all maps shown below are presented in a logarithmic intensity scale. Fig. 2a shows the evolution of the 002_R film reflection as seen on different projections (3D maps overview in Figure S1, Suppl. Info). The vertical Q_xQ_z projection corresponds to a slice following the $[110]^*_R$ direction, including the substrate reflection, while horizontal Q_xQ_y maps integrate a slice around the VO_2 film peak only. The diffuse inverted-V shape, already observed at 30 °C, combined with the horizontal Q_xQ_y projection, indicates that the VO_2 intensity is distributed in four main branches following the $[110]^*_R$ /$[1\text{-}10]^*_R$ directions in the horizontal plane, and pointing downwards at a certain angle with the vertical axis. As can be observed in Fig. 2a, the intensity maximum is in the central axis at Q_x=Q_y=0. This is consistent with the observation of the linear scan in Fig. 1a which indicates a single peak at the Q_z position expected for the strained M1 phase. The peak asymmetry, with a smoother intensity decay at lower 2θ angles, observed in that scan, thus can be attributed to the contribution of those diffuse intensity branches. At 30 °C one can only distinguish one peak corresponding to the M1 phase, but at 40 °C and 50 °C the R peak is observed in the $Q_{xy}Q_z$ maps at a higher Q_z value and Q_x=Q_y=0, indicating the transformation into the rutile phase. At this stage the M1 component progressively splits into four peaks away from the central Q_x=Q_y=0 position following the $[110]^*_R$ /$[1\text{-}10]^*_R$ directions, as indicated by yellow arrows. It can be observed that, upon increasing the temperature, the centroid positions of the M1 split components progressively shift along the inverted-V intensity traces. From the symmetric 002_R reflection one can only gather information about out-of-plane components, while a more complete insight into the in-plane components requires at least one reflection with H,K ≠ 0 components. Fig. 2b shows selected projections of 3D reciprocal space maps at the 112_R reflection. The vertical maps correspond to slices in two orthogonal directions: one following the $[110]^*_R$ axis ($Q_{xy}Q_z$ map), as above, and another one following the perpendicular $[1\text{-}10]^*_R$ axis ($Q_{x\text{-}y}Q_z$ map). The horizontal Q_xQ_y maps show again four main branches with projections following the $[110]^*_R$/$[1\text{-}10]^*_R$ directions. This crossed pattern is centered in the same (Q_x,Q_y) position as the TiO_2 substrate 112 reflection. Splitting of the M1 maximum along these branches is clear at 40 °C and 50 °C, (indicated with yellow arrows) but only incipient at 30 °C. In the horizontal maps, contrary to the splitting observed in the 002_R reflection, the branches following the $[110]^*_R$ direction show asymmetric splitting from the central (Q_x,Q_y) position: the centroid position indicated with the yellow arrow shows a larger shift than the opposite split component. Instead, along the $[1\text{-}10]^*_R$ direction, the splitting remains symmetric (as indicated by red arrows). This difference is

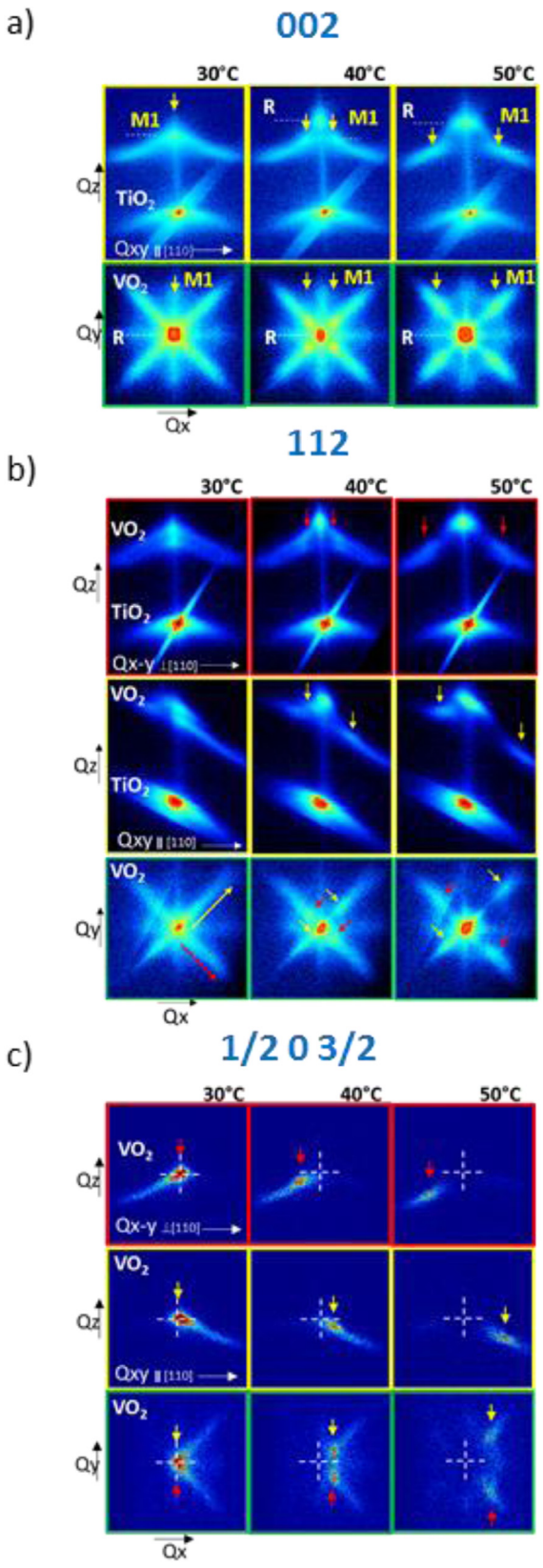

Fig. 2. XRD reciprocal space maps of different VO_2 reflections obtained at 30, 40 and 50 °C during the phase transition: (a) vertical $Q_{xy}Q_z$ and horizontal Q_xQ_y 2D projections of the 002_R reflection; (b) vertical $Q_{x\text{-}y}Q_z$, $Q_{xy}Q_z$ and horizontal Q_xQ_y 2D projections of the 112_R reflection; and (c) vertical $Q_{x\text{-}y}Q_z$, $Q_{xy}Q_z$ and horizontal Q_xQ_y projections of the 1/2 0 $3/2_R$ reflection. The horizontal projections contain only VO_2 film reflections. The arrows indicate the split M1 components (red and yellow arrows indicate symmetric and asymmetric splitting, respectively). $\Delta Qx,y$ corresponds to a range of $\pm 0.025 Å^{-1}$ for (a) and (b), and $\pm 0.015 Å^{-1}$ for (c). The complete T range, acquired with 5 °C steps, is depicted in Fig. S2, S3 and S4 (Suppl. Info) for the 002_R, 112_R and 1/2 0 $3/2_R$ reflections, respectively.

even clearer in the vertical cuts. While the $Q_{x\text{-}y}Q_z$ maps show a symmetric arrangement similar to that observed in the 002_R reflection, the $Q_{xy}Q_z$ map is clearly asymmetric already at 30 °C. The two branches seem to follow the same oblique direction, although the one pointing towards larger Q_{xy} values is clearly more elongated than the opposite one. With increasing temperature the centroids of the split components shift apart following the trajectory of the pre-existing branches, as indicated by yellow arrows. At each temperature the in-plane magnitude of the splitting is the same for both directions parallel and perpendicular to $[110]^*_R$ (distance between red or yellow arrows). However, their average position along Q_{xy} in the asymmetric branch (middle position between the two yellow arrows) is displaced from the central position.

The behaviour described above can be interpreted as follows. The progressive splitting of the M1 components is consistent with an increasing domain tilting, while the asymmetric displacement from the central Q_{xy} position is due to a progressive variation of the in-plane reticular spacing along the $[110]^*_R$ direction. Importantly, both distortions increase with the progress of the transition to the rutile phase. It is worth noting that the lowering of the Q_z position for both M1 components in the vertical maps shown in Fig. 2a and 2b, indicates an increase of the out-of-plane unit cell parameter, contrary to the elastic response expected for the in-plane tensile strain imposed by the substrate. In contrast with this behaviour, in all the maps, the corresponding R component (intense peak appearing above 30 °C at larger Q_z in vertical maps) does not show any significant change, while its in-plane parameter remains coherent with that of TiO_2 substrate. Altogether, these results point to the build-up of severe internal stresses which selectively affect the monoclinic phase embedded in the rutile film, and that the stress level increases as its volume fraction decays during the transition. The evolution of reciprocal space maps obtained around the 1/2 0 $3/2_R$ reflection is shown in Fig. 2c. This reflection, arising from the unit cell doubling caused by the V-V dimerization, can in principle be attributed to either the M1 or M2 structures. It can be indexed as either $30\bar{2}_{M1}$ or $130/\bar{1}30_{M2}$. As can be observed in Fig. 2c, at 30 °C it shows a main peak at the same (Q_x,Q_y) position than that expected for a perfectly coherent VO_2 film on the TiO_2 substrate, along with diffuse branches. However, the horizontal Q_xQ_y projection clearly defines a pattern of only two main branches, instead of four, along $[110]^*_R$ and $[1\text{-}10]^*_R$ directions. Because of the four-fold symmetry of the substrates, the appearance of M2 domains would imply the existence of a couple of $130/\bar{1}30_{M2}$ equal intensity reflections for each 1/2 0 $3/2_R$ position (following $(100)/(010)_R$ mirror planes). This would necessarily generate a four-branch arrangement at the position of each half-order reflection, which is not observed. Instead, a set of M1 domains arranged following the 4-fold symmetry of the substrate may consist of one single $30\bar{2}_{M1}$ reflection at each $\pm Q_x,\pm Q_y$ quadrant in reciprocal space, compatible with the experimental observations. Therefore, the main contribution to the observed half-order reflections comes from crystal domains compatible with the M1 structure. We note that a small proportion of T or M2 phases could generate mirror branches that could go unnoticed due to the weakness of this reflection. In fact, a close look at the 50 °C Q_xQ_y map shows a very weak signal attributable to such mirror branches but they are too fade to extract any conclusion.

An additional important observation in the horizontal Q_xQ_y map of the 1/2 0 $3/2_R$ reflection at 40 °C concerns the peak splitting, which is even more evident at 50 °C. Contrary to previous 002_R and 112_R vertical cuts shown in Fig. 2a and 2b, these maps do not show any intensity at the central (Q_x,Q_y) position. This confirms the previous assignment of the central position to the R phase. The corresponding vertical $Q_{x\text{-}y}Q_z$ and $Q_{xy}Q_z$ maps also show meaningful differences with respect to the 002_R and 112_R reflections. The split components (indicated by yellow and red ar-

rows) and the diffuse branches appear only in the higher Q_x part of the maps. Again, upon heating up, the centroid positions shift apart from central position following the corresponding branches trajectory. The explanation for the selection of the higher Q_{xy} trace follows in the next paragraph. Similar splitting was also observed in other reflections, like 101_R shown in Figure S5 (of suppl. Info).

3.2. Geometrical model for the coexistence of M1 and R phases

Before considering in detail the microstructure reflected by the above results, we first recall the ferroelastic properties of VO_2. From group theory, the number of symmetry-degenerated domain orientations is equal to the order of the prototypic point group (4/mmm, order 16) divided by the order of the ferroelastic point group (2/m, order 4) [32]. Therefore, in the M1 phase there are four equivalent domain orientations, which can be generated by 90° rotations around the c_R-axis, as illustrated in Fig. 3 a. The permissible, low index, wall orientations separating these domains are $(100)_R$, $(010)_R$, $(001)_R$, $(110)_R$ and $(1\text{-}10)_R$ (in addition, there is another set of permissible walls whose orientation depends on the values of the spontaneous strain components). [33] Due to the monoclinic shear, the clamping of monoclinic domains at the domain walls requires a tilt which further increases the number of orientation variants, as actually seen in diffraction experiments. For instance, for $\{110\}_R$ -type walls, A domains in Fig. 3a, rotate around the $[110]_R$ or $[1\text{-}10]_R$ directions to satisfy the clamping on the $(1\text{-}10)_R$ or $(110)_R$ planes, with adjacent B and D domains respectively, defining two new variants,

A' and A'', as depicted in Fig. 3b. In this way, eight M1 variants are generated. On the other hand, the tetragonal R phase remains epitaxially-oriented with respect to the TiO_2 substrate axes (as illustrated in the center of the sketch). From these considerations it is possible to anticipate the spot distribution arising from the coexistence of the different M1 variants in reciprocal space. A scheme of such arrangement is shown in Fig. 3c to 3f. As starting point, ignoring domain clamping at domain walls (i.e. c^*_R remains parallel to the $[001]_R$ direction). Fig. 3c shows a horizontal section of reciprocal space for one single set of ferroelastic A domains (red dots), which for simplicity includes only $01L_R$, $10L_R$ and $11L_R$ -type reflections (with L any integer number different from zero). The sketch also includes the half order reflection -1/2 0 $L/2_R$, which, as the 1/2 0 $3/2_R$ one measured in this study, is characteristic of the M1 structure. Each M1 variant will have a unique -1/2 0 $L/2_R$ set of reflections along the direction of the M1 shear distortion, related to the unit cell parameter doubling induced by the V-V dimerization.

As mentioned before, asymmetries in reciprocal space maps may be accounted for by applying a uniaxial compression perpendicular to the clamping rotation about the $[110]^*_R$ or $[1\text{-}10]^*_R$ axes (i.e. perpendicular to the domain walls). This compression is incorporated into the model as sketched in Fig. 3e for A'/A'' domains. The position of the spots in reciprocal space is shifted away from the corresponding rotation axis (in the direction of the arrows). This situation is the same for the rest of the B'/B'', C'/C'' and D'/D'' variants. The spot distribution resulting from the combined domain tilts and compression is depicted in Fig. 3f. Squared regions correspond to the areas analyzed in this work. This model is qualitatively consistent with the experimental observations of the symmetric crossed pattern in Q_xQ_y maps of the 002_R reflection (Fig. 2a), as well as of the asymmetric cross pattern in Q_xQ_y maps of the 112_R reflection (Fig. 2b). The model also reproduces the two-branch asymmetric Q_xQ_y maps of the 1/2 0 $3/2_R$ reflection observed in Fig. 2c.

Similarly, one can draw the model for the vertical projections of reciprocal space, as depicted in Fig. 4. In epitaxial domains with tetragonal structure, i.e.: with no monoclinic shear and no rotation from substrate plane, the out-of-plane and in-plane coordinates of

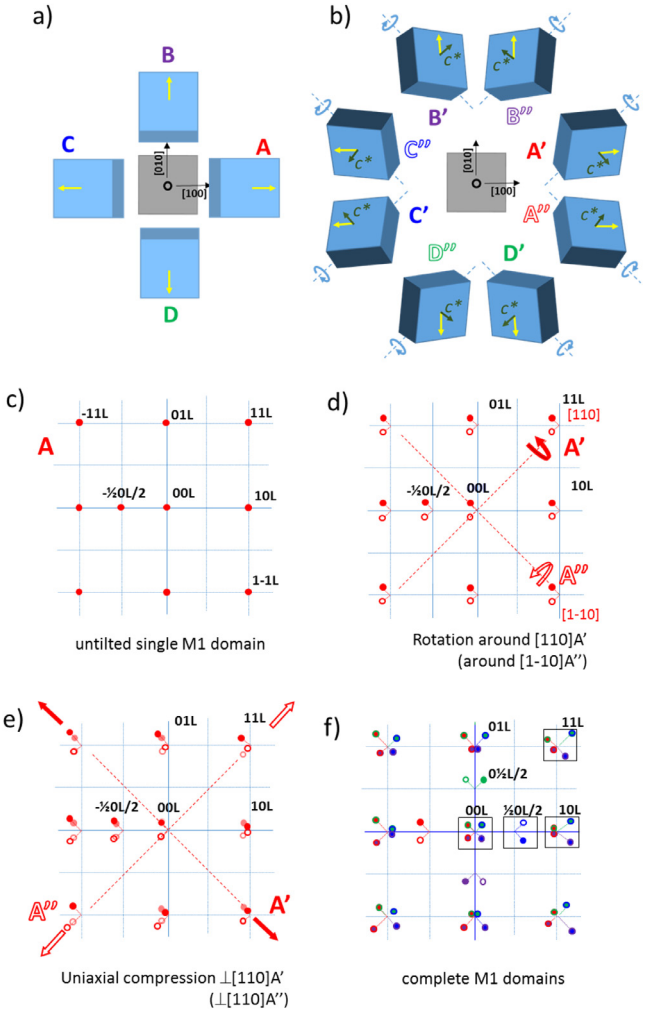

Fig. 3. (a) Top view sketch of the different variants of M1 domains arranged in four untilted ferroelastic domains (A, B, C and D) relative to the prototype R structure. The yellow arrows indicate the monoclinic shear direction along the $[100]_R$ or $[010]_R$ prototype axes for each domain. (b) Scheme of the eight different M1 variants obtained after rotation around the $[110]_R$ and $[1\text{-}10]_R$ directions, required to satisfy clamping on the $\{110\}_R$ domain walls. The yellow arrow corresponds to the tilt of the corresponding c^*_R-axis along either the $[110]_R$ or $[1\text{-}10]_R$ directions. (c) Schematics of an horizontal reciprocal space cut including a selection of HKL reflections for untilted A domains; (d) for A'/A'' tilted domains; and (e) including an additional uniaxial compression of A'/A'' domains along the $[110]^*_R$ and $[1\text{-}10]^*_R$ directions, respectively (note the shift in individual positions from previous tilted positions indicated by transparent symbols). (f) Complete arrangement of reflections for A'/A'', B'/B'', C'/C'' and D'/D'' variants (different colors are used for each variant).

the HHL and 00L reflections in the reciprocal space allow for direct determination of the corresponding cell parameters, as depicted in Fig. 4a. The appearance of a monoclinic shear distortion, with angle α_{shear}, induces a splitting of certain HKL reflections for the twin A'/A'' variants. If one considers that c^*_R remains perpendicular to the substrate surface for both domains, as in the sketch in Fig. 4b, the splitting is produced in the vertical direction of the HHL reflections, and the magnitude of the splitting should correspond to $2\alpha_{shear}$. Further rotation of the A'/A'' domains in opposite directions, with magnitude α_{rot}, shifts the HKL reflection positions accordingly, as depicted in Fig. 4c.

This shear and rotation, along with the uniaxial compression, also reproduce the main features observed in the vertical cuts of the 002_R, 112_R reflections, shown in Fig. 2, as well as that in 101_R reflection (i.e. the splitting and asymmetry of maps in Figure S5, in SI). However, despite the qualitative agreement, this interpreta-

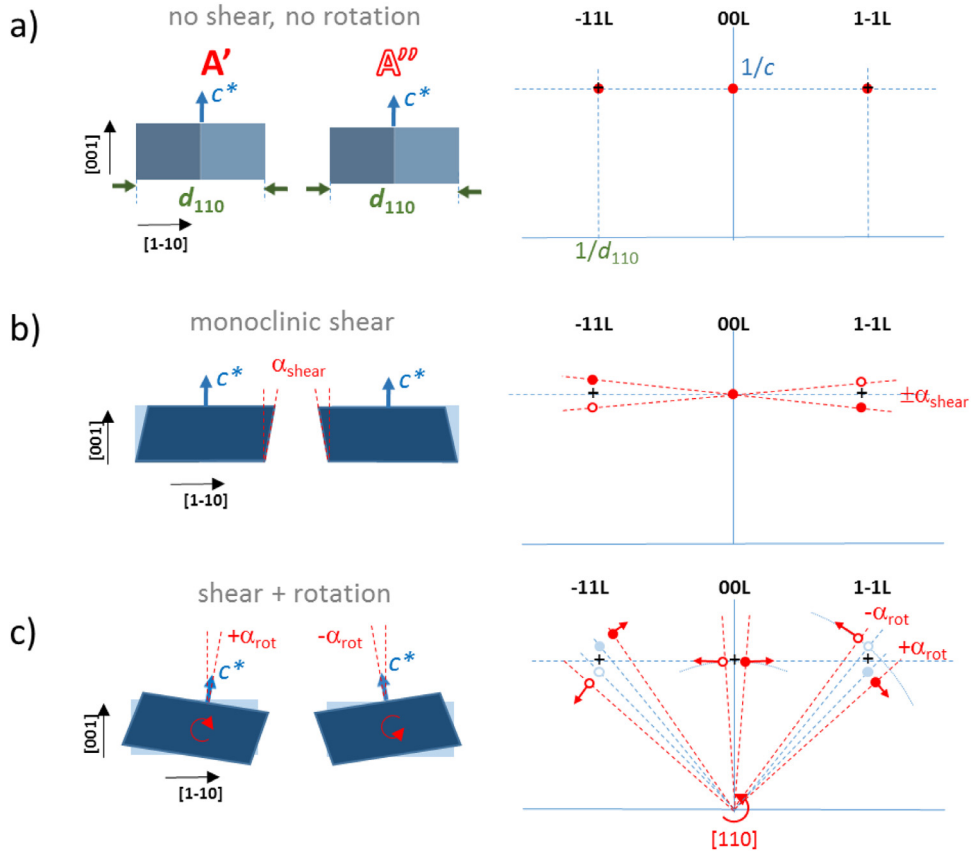

Fig. 4. Schematic of the distribution of 11L and 00L reflections in vertical projections of the reciprocal space for A'/A'' variants with different distortion: (a) no shear and no rotation of crystal domains, (b) with monoclinic shear angle α_{shear}; and (c) additional rotation of domains in opposite direction with angle α_{rot}. Filled and empty spots correspond to A' and A'' variants, respectively.

tion, based on a pure ferroelastic behaviour, fails to account for the actual strain and tilt values extracted from the diffraction data. In the next section, the analysis incorporates the martensitic character of the transformation by including the geometrical constrains associated to the coexistence of the R and M1 structures. By doing so, it is evidenced that these constrains are, in fact, responsible for a complex interplay between strain and phase stability which accurately accounts for the intensity distribution observed in the reciprocal space maps.

3.3. Martensitic character: Interplay between strain and phase stability

In order to check the validity of this model, we determined the out-of-plane and in-plane unit cell parameters for the M1 and R phases, as well as the monoclinic shear and domain tilt angles of the M1 domains, as a function of temperature up to 60 °C. These values were extracted from the main peak positions in the XRD maps assigned to the different domains according to the previously described model, and are collected in Fig. 5. Different reflections were analyzed: 002_R (in two different in-plane azimuthal angles, either parallel to $[100]^*_R$ or $[110]^*_R$), and $\bar{1}\bar{1}2_R$ (along $[110]^*_R$) or $\bar{1}03_R$ (along $[100]^*_R$) reflections. Essentially, the calculation directly extracts the rotation angle from the in-plane splitting of 002_R reflections. The rotation angle can be also calculated from the $\bar{1}\bar{1}2_R$ and $\bar{1}03_R$ reflections as the necessary tilt to bring twin variants to a common in-plane coordinate in reciprocal space. Therefore, the remaining vertical splitting corresponds uniquely to the monoclinic shear. The average in-plane and out-of-plane cell parameters are therefore calculated once the corresponding shear and rotation corrections are applied. More details of the calculation of the unit cell parameters are given in the supplementary info (Figure S6 and S7). Fig. 5a indicates the XRD intensity of both R and M1 components obtained from the corresponding 002_R maps, which can be taken as an estimate of the relative concentration of M1 and R phases in the film. At room temperature the film is apparently pure M1 and upon increasing temperature, the R fraction increases abruptly above 30 °C reaching a value of about 90 % already at 40 °C. Above this temperature the M1 phase is still present but in a much reduced amount. From the M1/R ratio one can consider that the transition takes place in a broad temperature range between 30 and 40 °C. This reduced transition temperature, well below T_c = 68 °C for bulk VO_2, results from the epitaxial strain on TiO_2(001) which stabilizes the rutile structure against the monoclinic one [11].

The measured out-of-plane unit cell parameters are depicted in Fig. 5b as extracted from the 002_R, 112_R, and 103_R reflections. The coincidence between the values extracted from these reflections is a proof of the validity model, except for the measurement at T= 35 °C, at the onset of transition, where there were difficulties in resolving the different M1 components and large errors are expected. At room temperature, out-of-plane c_R values of 2.854 Å and 2.837 Å were measured for M1 and R phases, respectively. These values are consistent with those measured from the linear scans of 002_R reflections in Fig. 1a. Up to 35 °C no substantial changes are observed, but above 35 °C a change in the slope of the out-of-plane expansion of the M1 phase is clearly observed. A qualitatively similar dependence was already observed in a previous report on epitaxial films of VO_2/TiO_2(001) [34]. In that T range the apparent thermal expansion coefficient derived from our data is

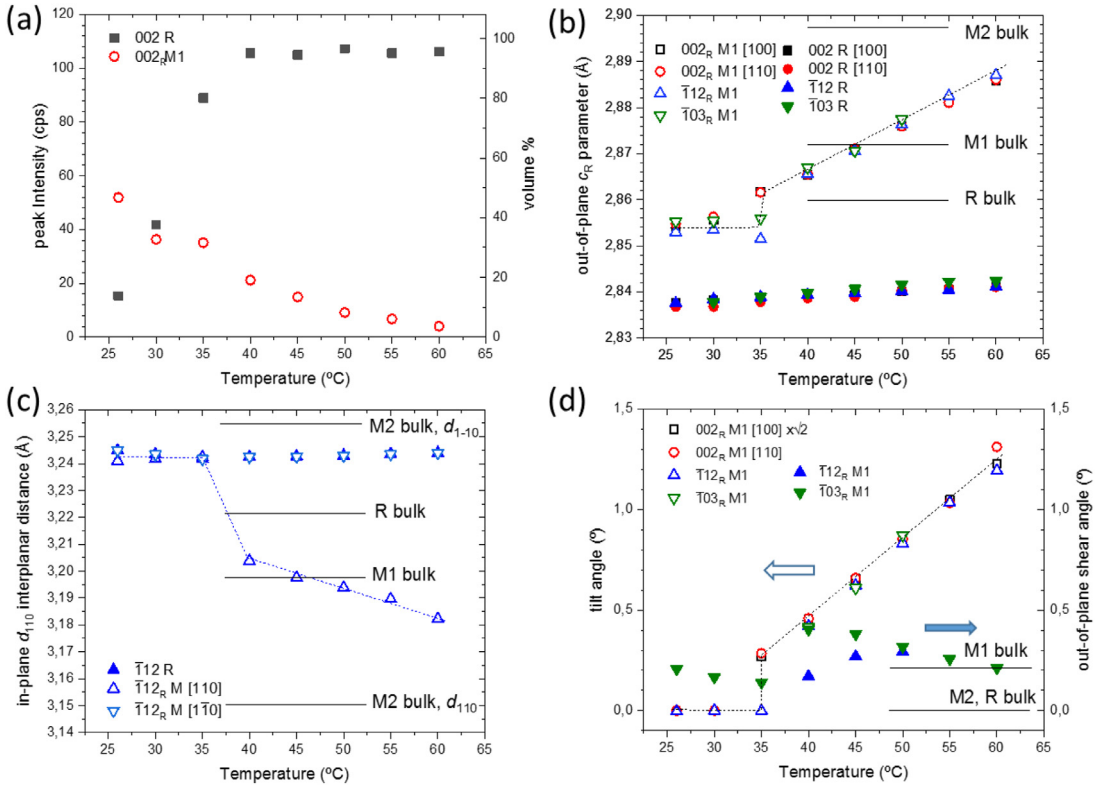

Fig. 5. Structural evolution of the R and M1 phases during the transition. (a) Intensity of 002_R contributions; (b) Out-of-plane cell parameters extracted from the 002_R, 112_R and 103_R reflections; (c) In-plane unit cell parameters extracted from the 112_R reflection; and (d) Tilt angles (empty symbols) and monoclinic shear angles (filled symbols) of M1 domains.

353 10^{-6} K^{-1}, which clearly contrasts with the much lower thermal expansion coefficient of about 55 10^{-6} K^{-1} measured for the R phase. A comparison with reported values for rutile VO_2, of about 30 10^{-6} K^{-1} [35,36], indicates that the thermal expansion measured here for epitaxial rutile VO_2 is not far from reported values of bulk samples. On the other hand, the out-of-plane M1 phase expansion considerably deviates from reported bulk values. In fact, at 60 °C, the M1 phase attains a c_R-axis parameter of about 2.887 Å, which surpasses the bulk value, c_R = 2.872 Å. [37] This expansion is contrary to the elastic response expected for the in-plane tensile strain imposed by the TiO_2 substrate, and should be related to a phase change rather than to thermal expansion. The corresponding in-plane unit cell parameters extracted from the positions of the different M1 components of the 112_R reflection are depicted in Fig. 5c. In the direction perpendicular to $[110]_R$, the M1 domains show an in-plane interplanar distance, $d_{1\text{-}10}$, similar to that of the R phase, of about 3.242 Å, which also matches that of the TiO_2 substrate as expected for a fully strained state. However, in the direction parallel to $[110]_R$, the interplanar d_{110} distance suffers a sudden compression of about -1.2 %, from 3.242 Å to 3.203 Å at 40 °C. Above this temperature it continues decreasing linearly down to 3.180 Å at 60 °C, well below the reported bulk value of d_{110} = 3.198 Å.[37] Therefore, the M1 phase changes from an in-plane tensile strained state to a compressive state along the $[110]_R$ direction, while it maintains a tensile strained value in the orthogonal $[1\text{-}10]_R$ direction. This large uniaxial in-plane distortion cannot be explained neither in terms of mere thermal expansion, nor as an elastic response to the biaxial epitaxial strain. Besides, if one looks at the M1 domain tilt angle derived from the splitting of the 002_R, 112_R and 103_R reflections from M1 phase along the $[110]_R$ direction, depicted in Fig. 5d, it is clear that below 30 °C there is no detectable tilt angle, while above 35 °C there is a sudden change followed by a linear increase reaching a maximum value of α_{rot}=1.25° at 60 °C, far exceeding α_{rot}=0.23° corresponding to $\{110\}_R$-type twin domains in the bulk M1 phase. This anomalous behavior clearly indicates that the observed domain tilting does not result from the twin structure expected for the ferroelastic M1 phase.

In order to get insights into the origin of the distortion, we decoupled the domain tilt angle from its corresponding monoclinic shear angle. Fig. 5d shows the shear angle values derived from the splitting of 112_R reflections (measured along $[110]^*_R$ direction), and of 103_R reflections (along $[100]^*_R$ direction). Below 35 °C the measured shear angles are about 0.2-0.3°, which do not deviate much from the monoclinic shear angle α_{shear} = 0.32° along the $[100]^*_R$ direction (0.23° if measured along $[110]^*_R$ direction) of the M1 bulk structure. However, above 35 °C, in the temperature interval dominated by the coexistence of M1 and R phases, the variations in shear strain evidence a discrepancy with both monoclinic M1 and M2 phases. Altogether these observations indicate that the larger the fraction of the rutile phase, the more pronounced the distortion of the remaining M1 domains, far from their bulk equilibrium structure. In fact, the enlargement of the c_R parameter observed in Fig. 5b, and the uniaxial compression along the $[110]_R$ direction, suggest a progressive transformation of the M1 structure towards the reported values of the M2 phase, as indicated in the graph (c_R=3.898 Å, and $d_{[110]}$=3.150 Å, $d_{[1\text{-}10]}$=3.255 Å [14]). Moreover, the progressive, rather than abrupt, evolution of the crystal structure is consistent with the formation of the transitional T phase, reported to bridge the M1 and M2 phases through a progressive dimerization of V ions [10].

3.4. Dynamical model of M1 and R phase coexistence

Fig. 6 shows the 002_R reflection, in a Q_xQ_z map (projection along the $[110]^*_R$ direction), obtained from a 50 nm thick film at

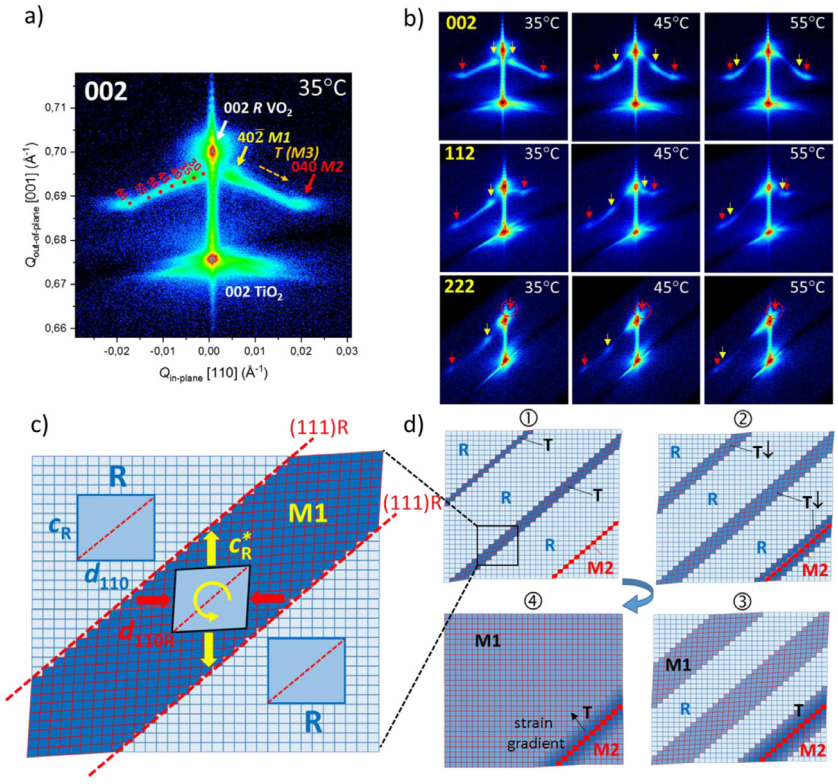

Fig. 6. a) XRD reciprocal space map of the 002_R reflection, obtained at 35 °C from a 50nm thick film, projected along the out-of-plane $[001]^*_R$ and in-plane $[110]^*_R$ directions. The arrows indicate the positions of the epitaxial R component, along with the tilted M1, T and M2 components forming the inverted-V shape. The red dots in the graph indicate the trajectory of the centroid position corresponding to the T domains between 30 to 60 °C. Note the clear definition of the M2 spot at the end of the arms (red arrows). b) Reciprocal space projections of the 002_R, 112_R and 222_R reflections (expressed in the rutile setting) along the out-of-plane $[001]^*_R$ and in-plane $[110]^*_R$ directions at increasing temperatures. The red arrows indicate the position of the tilted M2 components, while the yellow arrows point to the centroid positions of the evolving T-phase at different stages of the transformation, from M1 to M2. Note the asymmetry between the left and right arms at the 112_R and 222_R reflections. The red circles in the 222_R maps indicate the absence of the right arm for the M1 (and M2) components across the transition, which overlap with the R component, indicating matching between the R, M1, T, and M2 structures on the $(111)_R$ planes. c) Schematic detail of the relative orientation between the R and M1 phases with common matching $(111)_R$ planes, showing the tilt and compression along the $[110]_R$ direction of the M1 (T and M2). domains. d) Sequence (from ① to ④) of monoclinic phase nucleation and evolution through the M2 and T phases during cooling down from the rutile phase. Some parts in the vicinity of M2 domains retain a strain gradient accommodated in the T phase, ③, even when the film has fully transformed into the M1 ground state (T-phase strain gradient in ④).

35 °C, when the majority phase is already R but still a clear signal from M1 domains is observed. This map is very similar to that previously presented in Figure 2a for a thicker film, and shows the inverted V-shape with symmetric branches at both sides of the central axis at $Q_{[110]} = 0$. The splitting of M1 002_R peaks is already resolved at this temperature (indicated with a yellow arrow). Particularly apparent in this map is the existence of an intensity peak at the extreme positions of the diffuse branches (indicated with a red arrow), which is consistent with tilted domains with the unit cell parameters of the M2 phase (040_{M2} reflection). The continuous trace between the M1 and M2 reflections can be explained by the formation of a progressive transitional state in the T phase (indicated by orange labels). Thus, this observation indicates that even at room temperature, when the film has transformed to M1, there are still residual strain gradients corresponding to the frozen structural trajectory of the metastable T phase. The graph also shows superimposed the centroid positions of the split T components measured at different temperatures, from 30 to 60 °C, on the same sample. It is apparent that, as the temperature increases, the centroid positions of the split components follow exactly the same trajectory as the preexisting intensity traces caused by the reverse transformation during cooling from the growth temperature. This indicates that the structural path through the T phase is reversible.

Considering the martensitic character of the transition, it is reasonable to think that the contact between the R and M1 phases occurs on preferred crystallographic planes minimizing the coherency strains between the two structures. In this situation, the large difference between the unit cell parameters of the two phases is likely to result in the build-up of large stresses during cooling down across the phase transition. In this sense, it is interesting to note that the evolution of the 112_R M1 components in the $Q_{xy}Q_z$ and Q_xQ_y maps shown in Fig. 2b indicates that the peak closer to the central position along the $[110]^*_R$ direction shows a very small shift compared to the other components. This suggests the occurrence of an invariant R/M1 matching which constrains the rotation and distortion of M1 domains. In order to check this hypothesis, different HHL maps (H= 0, 1, 2, L =2) were measured on the 50nm thick film at T= 35, 45 and 55 °C. Fig. 6b shows vertical $Q_{xy}Q_z$ cuts of the 3D maps parallel to the $[110]^*_R$ direction. The maps show R (central axis) and M1 (inverted "V"-shape) components analogous to those previously shown in Fig. 2. $Q_{xy}Q_z$ maps of the 002_R reflection are symmetric, while the $Q_{xy}Q_z$ cuts of the 112_R and 222_R reflections show asymmetric branches. The yellow arrows indicate the evolution with temperature of the centroid positions of residual M1 tilted domains, similar to that observed in the 002_R reflection, while the red arrow corresponds to the extreme position of the tilted M2 domains. An interesting feature arises from the extent of the branches of these asymmetric $Q_{xy}Q_z$ maps. It is apparent that, in the 112_R reflection, the right branch is considerably reduced with respect to that observed in the 002_R maps and, for the 222_R reflection, the right branch is no

longer observed. This behavior is consistent with the occurrence of one set of $(111)_R$ planes belonging to the M1 phase, namely $(210)/(2\bar{1}0)_{M1}$, being parallel to the $(111)_R$ planes of the R phase, as shown in the scheme depicted in Fig. 6c, and with strain gradients developing perpendicularly to that contact plane. The same contact plane, $(111)_R$ // $(221)_{M2}$, has been previously shown to provide favorable matching between R and M2 domains in VO_2 microcrystals.[38] These are equivalent to the $(210)/(2\bar{1}0)_{M1}$ planes in the M1 structure, and therefore are expected to provide also favorable matching with the $(111)_R$ planes of the rutile structure. A calculation of the mismatch for different possible contact planes between the R and M1 bulk structures (see supplementary info, Fig. S8 and Table S1) indeed indicates that the best matching is obtained between the $(111)_R$ and $(210)/(2\bar{1}0)_{M1}$ planes, both equivalent in the pseudo-rutile representation of the M1 structure. Other interface orientations such as $(001)_R$ // $(010)_{M2}$ or $(021)_R$ // $(011)_{M2}$, equivalent to $(001)_R$ // $(20\text{-}1)_{M1}$ or $(021)_R$ // $(22\text{-}1)_{M1}$, respectively, also reported in [38] to produce a low mismatch between R and M2 in VO_2 microcrystals, were not observed in this case.

Upon heating, as rutile becomes the dominant phase, the minority M1 phase is assumed to be confined in increasingly smaller domains, which thus become elastically softer, capable to rotate and compress along the $[110]_R$ direction to keep the common $(111)_R$ planes. This situation is equivalent to that observed in other oxides with tetragonal structure, like mixed *c*/*a*-axis oriented $Pb(Zr,Ti)O_3$ thin films [39], where partial strain relaxation is achieved by domain tilting of the minority phase, resulting in different orientation variants. In this case, the four possible $\{111\}_R$ planes determine four orientational variants of the M1 phase, following the $<110>_R$ directions, and the different shear directions of the M1 domains along $<100>_R$ result in eight orientational variants fully equivalent to the model shown in Fig. 3b. Although the M1 domain arrangement scheme was introduced based on the possible existence of ferroelastic $\{110\}_R$-type walls between M1 domains, the present coupling between R and M1 domains reproduces the same pattern. However, the experimental values of the M1 domain tilt, up to α_{rot}=1.25°, indicate a much larger tilt of M1 domains, which is not compatible with the domain tilt caused by {110}R-type walls, limited to a maximum value of the shear strain of the monoclinic structure (α_{shear}=0.32°). Instead, domain tilt due to the coupling between $(111)_R$ planes in the R and M1 structures (and ultimately with M2) has much wider limits and nicely accounts for the experimental data.

Once established the structural constrains controlling the coexistence of the M1 and R phases this part discusses about the phase distribution and their evolution during transition. Any attempt to directly observe the different phases' distribution across the film surface by micro-Raman spectroscopy resulted non conclusive because of the large overlap with the TiO_2 substrate as well as the very subtle changes of the observable low frequency phonon modes in the M1, M2 and T structures (as explained in Fig. S10 in the supplementary information). However, based on the X-ray diffraction results, a model of the microstructural evolution across the phase transition can be sketched as shown in Fig. 6d. At a temperature well above the transition, the whole volume of the film corresponds to the rutile structure, fully strained by the TiO_2 substrate. Upon cooling down, at the onset of the transition, in ①, narrow M1 domains start to nucleate on the equivalent $(111)_R$ planes of the rutile structure. In fact, this mechanism is fully consistent with the transition being driven by V ion displacements perpendicular to those planes [40]. Their small volume makes them elastically softer with respect to the surrounding R matrix, and therefore the elastic energy increase due to the nucleation of the M1 phase within the R matrix can be partially released by rotating the formed nuclei around a common $[1\text{-}10]_R$ axis. However, this rotation of M1 domains does not accommodate the elastic strain in the direction of the tilt axis. Therefore, a uniaxial in-plane strain is induced onto the M1 nuclei along the $[1\text{-}10]_R$ direction, which can stabilize intermediate structures between M1 and M2 in the T phase by adjusting the out-of-plane and in-plane lattice parameters and domain rotation, generating a continuous track reflected in the diffuse intensity branches (Fig. 6 a), as depicted in sequence ① and ②. In fact, these are size effects associated to varying degrees of V dimerization. As the transition proceeds, in sequence ② to ③, T domains grow in size and become less elastic, with a concomitant reduction in domain rotation, progressively transforming into the equilibrium M1 structure. The transition is completed at about 30-35 °C, in sequence ④, when most of the film volume has transformed into the M1 phase. This transformation is fully reversible when increasing temperature above T_c.

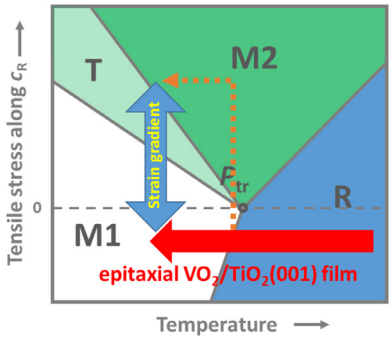

Fig. 7. Scheme of the VO_2 transformation path followed by the main film domains (thick red arrow) as well as interfacial regions (dashed orange line) across the c_R-axis strain vs Temperature phase diagram as reported in [11]. The blue arrow indicates the prevailing strain gradient at RT crossing stability regions of T and M2 phases.

As schematized in Fig. 6d, this mechanism carries the build-up of very high stresses along the $(111)_R$ planes, stabilizing M2 domains (depicted in red color). This implies a further elongation of the c_R axis (d_{001}=2.898 Å, +1.3 % relative to the R phase), which in turns requires a larger rotation with respect to the R matrix (up to α_{rot}=1.3°). To depict the phase transformation path Fig. 7 shows a scheme of the *c*-axis strain versus Temperature phase diagram, as reported in [11]. In this diagram the extent of T phase is enlarged for clarity. Note that the original in-plane biaxial tensile strain state of the film at the deposition temperature is expected to produce a compressive strain along *c*-axis (negative value). Therefore, upon cooling down VO_2 would follow a main path, below the triple point, where R transforms into M1 phase, without the formation of additional phases. However, once the first M1 domains are nucleated within the R matrix the build-up of uniaxial stresses counteract the epitaxial stress by inducing a c_R-axis expansion (positive strain value), turning some interfacial regions of the VO_2 film into M2 phase, as depicted in the vertical trajectory of the dashed line in the scheme. Further cooling down to RT would transform the M2 domains into the transitional T phase and eventually to the stable M1. The observation of the M2 phase at room temperature indicates that such stresses prevail after the transformation, and are responsible for the frozen strain gradients, bridging R and M1 structures through the T-phase, observed in virtually pure M1 films well below the transition temperature, in stage ④ of Fig. 6d. This mechanism explains the persistence of inverted V-shape intensity traces in the XRD reciprocal space maps. Finally, it is worthy to note that these phase transformation mechanisms very likely compete with crack formation in the relaxation of the high stress levels developed in these epitaxial films.

4. Conclusions

In summary, this work uncovers the interplay between intrinsic strains and phase stability in VO_2 epitaxial films deposited on $TiO_2(001)$ across its martensitic-like metal-insulator transition. 3D reciprocal space maps obtained from virtually perfect insulating M1 films exhibit weak diffuse intensity traces that represent the trajectories of Bragg reflections resulting from strong strain gradients frozen in the films after cooling from the growth temperature. In situ experiments show that, upon heating, these Bragg reflections follow the reverse trajectory along the preexisting intensity tracks, indicating a reversible behavior. The analysis of these traces shows that they result from a combination of normal strains and domain tilts which exceed by far those expected from the ferroelasticity of VO_2. This complex behavior is explained by considering the martensitic character of the transition and the subtle interplay between strain and phase stability in the proximity of the VO_2 triple point. Particularly, it is shown that the coexisting R and M1 phases share their common $(111)_R$ planes during the transition. This geometrical constrain, coupled with the epitaxial matching, results in domain tilts about the $<110>_R$ axes and the build-up of uniaxial compressive stresses perpendicular to them, causing the formation of the M2 phase. Moreover, it is shown that the diffuse intensity traces reflect varying degrees of V-V dimerization accommodated within the metastable triclinic T phase bridging the M1 and M2 structures. These results provide new insights into the microstructural consequences of the extreme sensitivity of VO_2 to strain, unveiling the existence of remnant dimerization disorder in virtually perfect insulating M1 films. This insight may have strong implications on the local electronic properties of the material, as well as for the understanding of the correlation between film microstructure and mechanical properties.

Declaration of Competing Interest

The authors declare that they have no known competing financial interests or personal relationships that could have appeared to influence the work reported in this paper.

Acknowledgments

This work was supported in part by the Spanish Ministry of Economy, Industry and Competitiveness (projects MAT2016-77100-C2-1-P and PID2019-108573GB-C21), and by the Catalan AGAUR agency (project: 2017-SGR-579). ICN2 is funded by the CERCA programme/Generalitat de Catalunya and by the Severo Ochoa programme (SEV-2017-0706). LR acknowledges the support of Severo Ochoa programme and ICN2 for her PhD grant. Part of the measurements were carried out at the KMC-II instrument at Helmholtz-Zentrum Berlin für Materialien und Energie. Besides, we would like to thank Dr. D. Többens for assistance during the KMC-II experiment. The research leading to this result has been partially supported by the project CALIPSO plus under the Grant Agreement 730872 from the EU Framework Programme for Research and Innovation HORIZON 2020. F.S. acknowledges the Spanish Ministry of Industry, Economy and Competitiveness (MINECO) for financial support through the “Severo Ochoa” programme for Centers of Excellence in R&D (SEV-2015-0496) and project no. RTI2018-098537-B-C21. The authors acknowledge the support of Dr. E. del Corro for the micro-Raman analysis of the films.

Supplementary materials

Supplementary material associated with this article can be found, in the online version, at doi:10.1016/j.actamat.2021.117336.

References

[1] F.J. Morin, Oxides which show a metal-to-insulator transition at the neel temperature, Phys. Rev. Lett. 3 (1959) 34–36, doi:10.1103/PhysRevLett.3.34.
[2] C.N. Berglund, H.J. Guggenheim, Electronic properties of VO_2 near the semiconductor-metal transition, Phys. Rev. 185 (1969) 1022–1033, doi:10.1103/PhysRev.185.1022.
[3] J.B. Goodenough, The two components of the crystallographic transition in VO_2, J. Solid State Chem. 3 (1971) 490–500, doi:10.1016/0022-4596(71)90091-0.
[4] A.S. Barker, H.W. Verleur, H.J. Guggenheim, Infrared optical properties of vanadium dioxide above and below the transition temperature, Phys. Rev. Lett. 17 (1966) 1286–1289, doi:10.1103/PhysRevLett.17.1286.
[5] T.D. Manning, I.P. Parkin, R.J.H. Clark, D. Sheel, M.E. Pemble, D. Vernadou, Intelligent window coatings: atmospheric pressure chemical vapour deposition of vanadium oxides, J. Mater. Chem. 12 (2002) 2936–2939, doi:10.1039/B205427M.
[6] D. Ruzmetov, G. Gopalakrishnan, C. Ko, V. Narayanamurti, S. Ramanathan, Three-terminal field effect devices utilizing thin film vanadium oxide as the channel layer, J. Appl. Phys. 107 (2010) 114516, doi:10.1063/1.3408899.
[7] M. Nakano, K. Shibuya, D. Okuyama, T. Hatano, S. Ono, M. Kawasaki, Y. Iwasa, Y. Tokura, Collective bulk carrier delocalization driven by electrostatic surface charge accumulation, Nature 487 (2012) 459–462, doi:10.1038/nature11296.
[8] Z. Yang, C. Ko, S. Ramanathan, Oxide electronics utilizing ultrafast metal-insulator transitions, Annu. Rev. Mater. Res. 41 (2011) 337–367, doi:10.1146/annurev-matsci-062910-100347.
[9] N.F. Quackenbush, H. Paik, M.J. Wahila, S. Sallis, M.E. Holtz, X. Huang, A. Ganose, B.J. Morgan, D.O. Scanlon, Y. Gu, F. Xue, L.-Q. Chen, G.E. Sterbinsky, C. Schlueter, T.-L. Lee, J.C. Woicik, J.-H. Guo, J.D. Brock, D.A. Muller, D.A. Arena, D.G. Schlom, L.F.J. Piper, Stability of the M2 phase of vanadium dioxide induced by coherent epitaxial strain, Phys. Rev. B. 94 (2016) 85105, doi:10.1103/PhysRevB.94.085105.
[10] J.P. Pouget, H. Launois, J.P. D'Haenens, P. Merenda, T.M. Rice, Electron localization induced by uniaxial stress in pure VO2, Phys. Rev. Lett. 35 (1975) 873–875, doi:10.1103/PhysRevLett.35.873.
[11] J. Cao, Y. Gu, W. Fan, L.Q. Chen, D.F. Ogletree, K. Chen, N. Tamura, M. Kunz, C. Barrett, J. Seidel, J. Wu, Extended mapping and exploration of the vanadium dioxide stress-temperature phase diagram, Nano Lett 10 (2010) 2667–2673, doi:10.1021/nl101457k.
[12] J.H. Park, J.M. Coy, T.S. Kasirga, C. Huang, Z. Fei, S. Hunter, D.H. Cobden, Measurement of a solid-state triple point at the metal–insulator transition in VO_2, Nature 500 (2013) 431–434, doi:10.1038/nature12425.
[13] J.P. Pouget, H. Launois, T.M. Rice, P. Dernier, A. Gossard, G. Villeneuve, P. Hagenmuller, Dimerization of a linear Heisenberg chain in the insulating phases of $V_{1-x}Cr_xO_2$, Phys. Rev. B. 10 (1974) 1801–1815, doi:10.1103/PhysRevB.10.1801.
[14] M. Marezio, D.B. McWhan, J.P. Remeika, P.D. Dernier, Structural aspects of the metal-insulator transitions in Cr-doped VO_2, Phys. Rev. B. 5 (1972) 2541–2551, doi:10.1103/PhysRevB.5.2541.
[15] J. Laverock, V. Jovic, A.A. Zakharov, Y.R. Niu, S. Kittiwatanakul, B. Westhenry, J.W. Lu, S.A. Wolf, K.E. Smith, Observation of Weakened V—V dimers in the monoclinic metallic phase of strained VO_2, Phys. Rev. Lett. 121 (2018) 256403, doi:10.1103/PhysRevLett.121.256403.
[16] F. Grandi, A. Amaricci, M. Fabrizio, Unraveling the Mott-Peierls intrigue in vanadium dioxide, Phys. Rev. Res. 2 (2020) 13298, doi:10.1103/PhysRevResearch.2.013298.
[17] F. Sandiumenge, L. Rodríguez, M. Pruneda, C. Magén, J. Santiso, G. Catalan, Metallic diluted dimerization in VO_2 tweeds, Adv. Mater. 33 (2021) 2004374, doi:10.1002/adma.202004374.
[18] A. Tselev, V. Meunier, E. Strelcov, W.A. Shelton, I.A. Luk'yanchuk, K. Jones, R. Proksch, A. Kolmakov, S.V Kalinin, Mesoscopic metal−insulator transition at Ferroelastic domain walls in VO_2, ACS Nano 4 (2010) 4412–4419, doi:10.1021/nn1004364.
[19] A. Tselev, E. Strelcov, I.A. Luk'yanchuk, J.D. Budai, J.Z. Tischler, I.N. Ivanov, K. Jones, R. Proksch, S.V Kalinin, A. Kolmakov, Interplay between Ferroelastic and metal−insulator phase transitions in strained quasi-two-dimensional VO_2 Nanoplatelets, Nano Lett 10 (2010) 2003–2011, doi:10.1021/nl1008794.
[20] J. Wu, Q. Gu, B.S. Guiton, N.P. de Leon, L. Ouyang, H. Park, Strain-induced self organization of metal−insulator domains in single-crystalline VO_2 Nanobeams, Nano Lett 6 (2006) 2313–2317, doi:10.1021/nl061831r.
[21] J. Cao, E. Ertekin, V. Srinivasan, W. Fan, S. Huang, H. Zheng, J.W.L. Yim, D.R. Khanal, D.F. Ogletree, J.C Grossman, J Wu, Strain engineering and one-dimensional organization of metal-insulator domains in single-crystal vanadium dioxide beams, Nat. Nano. 4 (2009) 732–737, doi:10.1038/nnano.2009.266.
[22] J.I. Sohn, H.J. Joo, D. Ahn, H.H. Lee, A.E. Porter, K. Kim, D.J. Kang, M.E. Welland, Surface-stress-induced mott transition and nature of associated spatial phase transition in single crystalline VO_2 nanowires, Nano Lett 9 (2009) 3392–3397, doi:10.1021/nl900841k.
[23] S. Zhang, J.Y. Chou, L.J. Lauhon, Direct correlation of structural domain formation with the metal insulator transition in a VO_2 Nanobeam, Nano Lett 9 (2009) 4527–4532, doi:10.1021/nl9028973.
[24] M. Liu, S. Xie, L. Wei, M. Galluzzi, Y. Li, Q. Wang, X. Zhou, Y. Wang, J. Li, Quantitative functional imaging of VO2 metal-insulator transition through intermediate M2 phase, Acta Mater 195 (2020) 720–727, doi:10.1016/j.actamat.2020.06.014.

[25] L. Vidas, C.M. Günther, T.A. Miller, B. Pfau, D. Perez-Salinas, E. Martínez, M. Schneider, E. Gührs, P. Gargiani, M. Valvidares, R.E. Marvel, K.A. Hallman, R.F. Haglund, S. Eisebitt, S. Wall, Imaging Nanometer phase coexistence at defects during the insulator–metal phase transformation in VO2 thin films by resonant soft X-ray holography, Nano Lett 18 (2018) 3449–3453, doi:10.1021/acs.nanolett.8b00458.
[26] Y. Ji, Y. Zhang, M. Gao, Z. Yuan, Y. Xia, C. Jin, B. Tao, C. Chen, Q. Jia, Y. Lin, Role of microstructures on the M1-M2 phase transition in epitaxial VO(2) thin films, Sci. Rep. 4 (2014) 4854, doi:10.1038/srep04854.
[27] L. Rodríguez, E. del Corro, M. Conroy, K. Moore, F. Sandiumenge, N. Domingo, J. Santiso, G. Catalan, Self-pixelation through fracture in VO_2 thin films, ACS Appl. Electron. Mater. 2 (5) (2020) 1433–1439, doi:10.1021/acsaelm.0c00199.
[28] K. Kawatani, H. Takami, T. Kanki, H. Tanaka, Metal-insulator transition with multiple micro-scaled avalanches in VO_2 thin film on TiO_2(001) substrates, Appl. Phys. Lett. 100 (2012) 173112, doi:10.1063/1.4709429.
[29] T. Yajima, Y. Ninomiya, T. Nishimura, A. Toriumi, Drastic change in electronic domain structures via strong elastic coupling in VO_2 films, Phys. Rev. B. 91 (2015) 205102, doi:10.1103/PhysRevB.91.205102.
[30] M. Liu, A.J. Sternbach, M. Wagner, T.V Slusar, T. Kong, S.L. Bud'ko, S. Kittiwatanakul, M.M. Qazilbash, A. McLeod, Z. Fei, E. Abreu, J. Zhang, M. Goldflam, S. Dai, G.-X. Ni, J. Lu, H.A. Bechtel, M.C. Martin, M.B. Raschke, R.D. Averitt, S.A. Wolf, H.-T. Kim, P.C. Canfield, D.N. Basov, Phase transition in bulk single crystals and thin films of VO_2 by nanoscale infrared spectroscopy and imaging, Phys. Rev. B. 91 (2015) 245155, doi:10.1103/PhysRevB.91.245155.
[31] J.-P. Pouget, Basic aspects of the metal{\textendash}insulator transition in vanadium dioxide VO_2: a critical review, Comptes Rendus. Phys. 22 (2021) 37–87, doi:10.5802/crphys.74.
[32] K. Aizu, Possible species of ferromagnetic, ferroelectric, and Ferroelastic crystals, Phys. Rev. B. 2 (1970) 754–772, doi:10.1103/PhysRevB.2.754.
[33] J. Sapriel, Domain-wall orientations in ferroelastics, Phys. Rev. B. 12 (1975) 5128–5140, doi:10.1103/PhysRevB.12.5128.
[34] H. Qiu, M. Yang, Y. Dong, H. Xu, B. Hong, Y. Gu, Y. Yang, C. Zou, Z. Luo, C. Gao, The tetragonal-like to rutile structural phase transition in epitaxial VO_2 /TiO_2 (001) thick films, New J. Phys. 17 (2015) 113016, doi:10.1088/1367-2630/17/11/113016.
[35] D. Kucharczyk, T. Niklewski, Accurate X-ray determination of the lattice parameters and the thermal expansion coefficients of VO_2 near the transition temperature, J. Appl. Crystallogr. 12 (1979) 370–373, doi:10.1107/S0021889879012711.
[36] K.V.K. Rao, S.V.N. Naidu, L. Iyengar, Thermal expansion of tetragonal phase of VO_2, J. Phys. Soc. Japan. 23 (1967) 1380–1382, doi:10.1143/JPSJ.23.1380.
[37] G. Andersson, J. Paju, W. Lang, W. Berndt, Studies on vanadium oxides. I. Phase analysis, Acta Chem. Scand. 8 (1954) 1599–1606, doi:10.3891/acta.chem.scand.08-1599.
[38] J.D. Budai, A. Tselev, J.Z. Tischler, E. Strelcov, A. Kolmakov, W.J. Liu, A. Gupta, J. Narayan, In situ X-ray microdiffraction studies inside individual VO_2 microcrystals, Acta Mater 61 (2013) 2751–2762, doi:10.1016/j.actamat.2012.09.074.
[39] K.S. Lee, J.H. Choi, J.Y. Lee, S. Baik, Domain formation in epitaxial Pb(Zr,Ti)O_3 thin films, J. Appl. Phys. 90 (2001) 4095–4102, doi:10.1063/1.1404424.
[40] J.D. Budai, J. Hong, M.E. Manley, E.D. Specht, C.W. Li, J.Z. Tischler, D.L. Abernathy, A.H. Said, B.M. Leu, L.A. Boatner, R.J. McQueeney, O. Delaire, Metallization of vanadium dioxide driven by large phonon entropy, Nature 515 (2014) 535–539, doi:10.1038/nature13865.